

The complete set of solutions of the geodesic equations in the space-time of a Schwarzschild black hole pierced by a cosmic string

Eva Hackmann ^{(a),*} Betti Hartmann ^{(b),†} Claus Lämmerzahl ^{(a),‡} and Parinya Sirimachan ^{(b),§}

^(a) *ZARM, Universität Bremen, Am Fallturm, 28359 Bremen, Germany*

^(b) *School of Engineering and Science, Jacobs University Bremen, 28759 Bremen, Germany*

(Dated: July 25, 2018)

We study the geodesic equations in the space-time of a Schwarzschild black hole pierced by an infinitely thin cosmic string and give the complete set of analytical solutions of these equations for massive and massless particles, respectively. The solutions of the geodesic equations can be classified according to the particle's energy and angular momentum, the ratio between the component of the angular momentum aligned with the axis of the string and the total angular momentum, the deficit angle of the space-time and as well the horizon radius (or mass) of the black hole. For bound orbits of massive test particles we calculate the perihelion shift, we discuss light deflection and comment on the Newtonian limit.

PACS numbers: 04.20.Jb, 02.30.Hq

I. INTRODUCTION

The motion of test particles (both massive and massless) provides the only experimentally feasible way to study the gravitational fields of objects such as black holes. Predictions about observable effects (light deflection, gravitational time-delay, the perihelion shift and the Lense-Thirring effect) can be made and compared with observations. Geodesics in black hole space-times in 4 dimensional Schwarzschild space-time [1] and Kerr and Kerr–Newman space-time [2] have been discussed extensively. This has been extended to the cases of Schwarzschild–de–Sitter space-times [3] as well as to spherically symmetric higher dimensional space-times [4]. Recently also the general solution to the geodesic equation in 4 dimensional Kerr–de–Sitter [5] and even general Plebanski–Demianski space-times without acceleration has been found [6].

Cosmic strings have gained a lot of renewed interest over the past years due to their possible connection to string theory [7]. These are topological defects [8] that could have formed in one of the numerous phase transitions in the early universe due to the Kibble mechanism. Inflationary models resulting from string theory (e.g. brane inflation) predict the formation of cosmic string networks at the end of inflation [9].

Different space-times containing cosmic strings have been discussed in the past. This study has mainly been motivated by the pioneering work of Bach and Weyl [10] describing a pair of black holes held apart by an infinitely thin strut. This solution has later been reinterpreted in terms of cosmic strings describing a pair of black holes held apart by two cosmic strings extending to infinity in opposite direction. Consequently, a cosmic string piercing a Schwarzschild black hole has also been discussed, both in the thin string limit [11] – where an analytic solution can be given – as well as using the full U(1) Abelian-Higgs model [12, 13], where only numerical solutions are available. In the latter case, these solutions have been interpreted to represent black hole solutions with long range “hair” and are thus counterexamples to the No hair conjecture which states that black holes are uniquely characterized by their mass, charge and angular momentum. Interestingly, the solution found in [11] is a Schwarzschild solution which however differs from the standard spherically symmetric case by the replacement of the angular variable ϕ by $\beta\phi$, where the parameter β is related to the deficit angle by $\Delta = 2\pi(1 - \beta)$. In this sense, the space-time is thus not uniquely determined by the mass, but is described by the mass *and* deficit angle parameter β .

Schwarzschild black holes pierced by cosmic strings could have formed in phase transitions in the early universe. One possibility would be that the Coulomb field of a charged static, spherically symmetric black hole becomes confined within a flux tube during such a phase transition. Interestingly, this space-time has also been used to describe the exterior space-time of the sun taking into account departures from perfect spherical symmetry [14].

*Electronic address: hackmann@zarm.uni-bremen.de

†Electronic address: b.hartmann@jacobs-university.de

‡Electronic address: laemmerzahl@zarm.uni-bremen.de

§Electronic address: p.sirimachan@jacobs-university.de

In order to understand details of gravitational fields of massive objects and to be able to predict observational consequences, it is important to understand how test particles move in these space-times.

Geodesics in the space-time of a Schwarzschild black hole pierced by a straight cosmic string have first been investigated in [15]. Spherical geodesics, i.e. geodesics in 3 spatial dimensions with constant radius r as well as perturbations about spherical orbits in this space-time have been discussed in [16] and it has been observed that the angular momentum precesses around the symmetry axis of the cosmic string. The geodesics have also been discussed in [17] using the Hamilton-Jacobi formalism. However, neither [16] nor [17] provide a systematic study of all possible geodesics. The crucial point about the solutions of the geodesic equations is that elliptic integrals have to be solved which was neither attempted in [16] nor [17].

The aim of this paper is to determine the *complete set* of analytic solutions of the geodesic equations in the space-time of a Schwarzschild black hole pierced by a cosmic string and to derive analytical expressions for observable effects which can be used for astrophysical searches for such cosmic strings.

Our paper is organized as follows: in Section II, we give the geodesic equations and discuss the effective potential. In Section III, we classify the solutions and give examples for each class. In particular we discuss the effect of the conical deficit on the geodesics. Section IV contains a short discussion about the Newtonian limit, while we conclude in Section V.

II. THE GEODESIC EQUATIONS

We consider the geodesic equation

$$\frac{d^2 x^\mu}{ds^2} + \Gamma_{\rho\sigma}^\mu \frac{dx^\rho}{ds} \frac{dx^\sigma}{ds} = 0, \quad (1)$$

where $\Gamma_{\rho\sigma}^\mu$ denotes the Christoffel symbol given by

$$\Gamma_{\rho\sigma}^\mu = \frac{1}{2} g^{\mu\nu} (\partial_\rho g_{\sigma\nu} + \partial_\sigma g_{\rho\nu} - \partial_\nu g_{\rho\sigma}) \quad (2)$$

and s is an affine parameter such that for time-like geodesics $ds^2 = g_{\mu\nu} dx^\mu dx^\nu$ corresponds to proper time. The explicit form of the metric that we are studying in this paper is the metric of a Schwarzschild black hole pierced by a cosmic string [11] :

$$ds^2 = \Sigma dt^2 - \Sigma^{-1} dr^2 - r^2 (d\theta^2 + \beta^2 \sin^2 \theta d\phi^2) \quad \text{with} \quad \Sigma = 1 - \frac{2m}{r}. \quad (3)$$

This metric describes a spherically symmetric static space-time with a conical deficit angle given by $2\pi(1 - \beta)$ and an event horizon at the Schwarzschild radius $r_s = 2m$. The deficit angle Δ is directly proportional to the energy per unit length μ , which itself is equal to the tension of the string: $\Delta = 2\pi(1 - \beta) = 8\pi G\mu$. In addition we have $m = MG$, where G is Newton's constant. Note that M is a parameter that is related to the physical mass M_{phys} of the black hole by $M_{\text{phys}} = \beta M$ [16] and can hence only be interpreted as the mass of the black hole if $\beta = 1$. M_{phys} is observable through the measurement of the event horizon radius by $M_{\text{phys}} = (\beta r_s)/(2G)$.

The Lagrangian \mathcal{L} for a point particle in the space-time (3) reads :

$$\begin{aligned} \mathcal{L} &= \frac{1}{2} g_{\mu\nu} \frac{dx^\mu}{ds} \frac{dx^\nu}{ds} = \frac{1}{2} \varepsilon \\ &= \frac{1}{2} \left[\left(1 - \frac{2m}{r}\right) \left(\frac{dt}{ds}\right)^2 - \left(1 - \frac{2m}{r}\right)^{-1} \left(\frac{dr}{ds}\right)^2 - r^2 \left(\left(\frac{d\theta}{ds}\right)^2 + \beta^2 \sin^2 \theta \left(\frac{d\phi}{ds}\right)^2 \right) \right], \end{aligned} \quad (4)$$

where $\varepsilon = 0$ for massless particles and $\varepsilon = 1$ for massive particles, respectively.

The constants of motion are the energy E and the component of the angular momentum of the particle that is aligned with the axis of the string (here the z -axis) L_z [16] :

$$E = \left(1 - \frac{2m}{r}\right) \frac{dt}{ds} = \text{constant}, \quad (5)$$

$$L_z = r^2 \beta \sin^2 \theta \frac{d\phi}{ds} = \text{constant}. \quad (6)$$

In addition

$$|\vec{L}|^2 \equiv L^2 = \left(\frac{d\theta}{ds} \right)^2 r^4 + \frac{L_z^2}{\sin^2 \theta} = \text{constant} . \quad (7)$$

Here $\vec{L} = (L_x, L_y, L_z)$ is the angular momentum vector, where

$$L_x = -r^2 \sin(\beta\phi) \frac{d\theta}{ds} - \beta r^2 \cos(\beta\phi) \cos \theta \sin \theta \frac{d\phi}{ds} \quad (8)$$

and

$$L_y = r^2 \cos(\beta\phi) \frac{d\theta}{ds} - \beta r^2 \sin(\beta\phi) \cos \theta \sin \theta \frac{d\phi}{ds} . \quad (9)$$

The modulus of the angular momentum is always conserved, however the direction of the angular momentum is only conserved for $\beta = 1$, i.e. in the “pure” Schwarzschild case.

Note that if we had used the Hamilton-Jacobi formalism here, the integration constant appearing in the separation of the equations –the so-called Carter constant– would have been equal to $L^2 - L_z^2$.

From variation of (4) and using the constants of motion, we obtain the geodesic equations :

$$\dot{t}^2 = E^2 \left(1 - \frac{2m}{r} \right)^{-2} , \quad (10)$$

$$\dot{r}^2 = E^2 - \left(\frac{L^2}{r^2} + \varepsilon \right) \left(1 - \frac{2m}{r} \right) , \quad (11)$$

$$\dot{\theta}^2 = \frac{L^2}{r^4} - \frac{L_z^2}{r^4 \sin^2 \theta} , \quad (12)$$

$$\dot{\phi}^2 = \frac{L_z^2}{\beta^2 r^4 \sin^4 \theta} , \quad (13)$$

where here and in the following the dot denotes the derivative with respect to the affine parameter s .

A. Effective potentials

Equations (11) and (12) can be rewritten in terms of effective potentials as follows:

$$\frac{1}{2} \dot{r}^2 + V_{\text{eff}}(r) = \frac{E^2 - \varepsilon}{2} , \quad r^4 \dot{\theta}^2 + V_{\text{eff}}(\theta) = L^2 , \quad (14)$$

where

$$V_{\text{eff}}(r) = -\varepsilon \frac{m}{r} + \frac{L^2}{2r^2} - \frac{L^2 m}{r^3} , \quad V_{\text{eff}}(\theta) = \frac{L_z^2}{\sin^2 \theta} . \quad (15)$$

The effective potential $V_{\text{eff}}(r)$ is exactly the same as that in the “pure” Schwarzschild case. Since $L^2 \geq V_{\text{eff}}(\theta)$, the θ motion is restricted:

$$\arcsin \left(\frac{L_z}{L} \right) \leq \theta \leq \pi - \arcsin \left(\frac{L_z}{L} \right) . \quad (16)$$

Apparently, for $L_z = L$, the motion occurs in the equatorial plane, i.e. $\theta = \pi/2$.

B. $r(\theta)$ and $r(\phi)$ motion

In the following, we will be mainly interested in the radial motion, i.e. we will solve the geodesic equations for $r(\theta)$ and $r(\phi)$. In order to do that we first have to eliminate the angular variable θ from (13). By dividing (12) by (13) we find [16]:

$$\frac{d\theta}{d\phi} = \beta \sin \theta \sqrt{k^2 \sin^2 \theta - 1} , \quad (17)$$

where $k^2 = (L/L_z)^2$. This can be solved to give [16]:

$$\cot^2 \theta = (k^2 - 1) \sin^2(\beta\phi) . \quad (18)$$

Using (18), (11), (13) and (12) we find:

$$\left(\frac{dr}{d\theta}\right)^2 = \frac{E^2 - \left(\frac{L^2}{r^2} + \varepsilon\right) \Sigma}{L^2 \sin^2 \theta - L_z^2} r^4 \sin^2 \theta \quad (19)$$

and

$$\left(\frac{dr}{d\phi}\right)^2 = \frac{E^2 - \left(\frac{L^2}{r^2} + \varepsilon\right) \Sigma}{L_z^2} \frac{\beta^2 r^4}{((k^2 - 1) \sin^2(\beta\phi) + 1)^2} . \quad (20)$$

Orbits with $\phi = \text{constant}$ are exactly the same as in the Schwarzschild case ($\beta = 1$), while for orbits with $\phi \neq \text{constant}$ the presence of the deficit angle influences the shape of the orbits significantly. The orbits are in general non-planar (except for the case $L_z = L$) and lie in a plane that has \vec{L} as its normal. Since \vec{L} is not conserved, this plane precesses [16].

In [16], the simplest case of non-planar orbits, namely spherical orbits and perturbations around spherical orbits have been discussed. Here, we want to give the complete set of possible orbits in this space-time and discuss all related observables.

C. Classification of solutions

Using the new variable $z = \frac{2m}{r} - \frac{1}{3}$ and introducing

$$\lambda = \frac{4m^2}{L^2} , \quad \mu = E^2 , \quad k = \frac{L}{L_z} \quad (21)$$

we find from (19) and (20) using (18):

$$\frac{dz}{\sqrt{P(z)}} = \frac{1}{2} \left(1 - \frac{1}{k^2 \sin^2 \theta}\right)^{-1/2} d\theta , \quad (22)$$

$$\frac{dz}{\sqrt{P(z)}} = \frac{1}{2} \beta k \frac{1}{(k^2 - 1) \sin^2(\beta\phi) + 1} d\phi , \quad (23)$$

where the third order polynomial $P(z)$ is given by

$$P(z) = 4z^3 - g_2 z - g_3 , \quad g_2 = 4 \left(\frac{1}{3} - \varepsilon \lambda\right) , \quad g_3 = 4 \left(\frac{2}{27} + \frac{2}{3} \varepsilon \lambda - \lambda \mu\right) \quad (24)$$

This is exactly the polynomial that appears in the case of the Schwarzschild solution and the classification of solutions is analogue. The main difference to the “pure” Schwarzschild case is that we have non-trivial integrals on the rhs of (22), (23). For a given k and β , the solutions can hence be classified according to the choice of μ and λ . Obviously, there are only solutions for $P(z) > 0$. Hence, we can classify solutions according to the zeros of the characteristic polynomial $P(z)$ and integrate (22), (23) for those z for which $P(z) > 0$. Note that in addition we can only integrate for $z \geq -1/3$ such that $r \geq 0$. Depending on the sign of the discriminant of $P(z)$ which is given by $D = g_2^3 - 27g_3^2$, the polynomial has either three real zeros ($D > 0$), one real zero ($D < 0$) or up to two real zeros for $D = 0$ which we will denote by e_1, e_2 and e_3 where $e_1 \leq e_2 \leq e_3$ in the following. This is illustrated in Fig.1 (left) for massive test particles ($\varepsilon = 1$), where the shaded regions I and II correspond to positive D , the boundary of the shaded region corresponds to $D = 0$ and the unshaded regions III and IV correspond to negative D . Note that $D > 0$ only if $\lambda < 1/3$ and $\mu > 8/9$. We also give the corresponding plot for massless test particles ($\varepsilon = 0$) in Fig.1 (right). The shaded region corresponds to $D > 0$, the unshaded region to $D < 0$ and the full boundary of the shaded region to $D = 0$. Note that $D > 0$ ($D < 0$) for $\lambda\mu < 4/27$ ($\lambda\mu > 4/27$) and that $D = 0$ for $\lambda\mu = 4/27$ or $\lambda\mu = 0$.

Comparing with (14), $D > 0$ corresponds to the case for which $V_{\text{eff}}^{\min} < \frac{E^2 - \varepsilon}{2} < V_{\text{eff}}^{\max}$, i.e. the total “energy” $\frac{E^2 - \varepsilon}{2}$ of the particle is smaller than the maximum V_{eff}^{\max} and larger than the minimum V_{eff}^{\min} of the effective potential $V_{\text{eff}}(r)$. For $D < 0$ then $\frac{E^2 - \varepsilon}{2} < V_{\text{eff}}^{\min}$ or $\frac{E^2 - \varepsilon}{2} > V_{\text{eff}}^{\max}$, while for $D = 0$, $\frac{E^2 - \varepsilon}{2} = V_{\text{eff}}^{\min}$ or $\frac{E^2 - \varepsilon}{2} = V_{\text{eff}}^{\max}$.

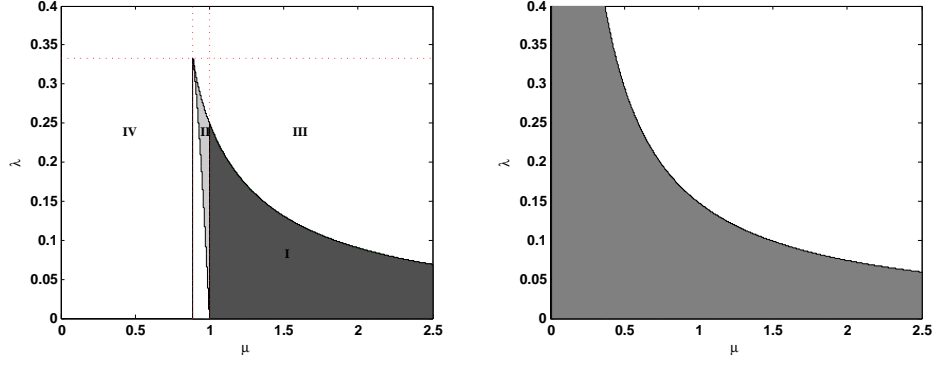


FIG. 1: The regions corresponding to positive, negative and zero discriminant D in the $\lambda - \mu$ plane for massive test particles (left) and massless test particles (right), respectively. For massive test particles the shaded regions I and II correspond to positive discriminant ($D > 0$), the unshaded regions III and IV correspond to negative discriminant ($D < 0$) and the boundary between the two regions to zero discriminant $D = 0$. The vertical line at $\mu = 1$ separates the motion of massive particles ($\varepsilon = 1$) with $\mu - \varepsilon > 0$ and $\mu - \varepsilon < 0$, respectively. For massless test particles, the shaded region corresponds to $D > 0$, the unshaded region to $D < 0$ and the full boundary of the $D > 0$ region to $D = 0$.

III. SOLUTIONS OF THE GEODESIC EQUATIONS

We can integrate (22)

$$g(\theta) \equiv \frac{1}{2} \left[\arcsin \left(\frac{\cos \theta}{\sqrt{1 - k^{-2}}} \right) - \arcsin \left(\frac{\cos \theta_0}{\sqrt{1 - k^{-2}}} \right) \right] = \int_{z_0}^{z(\theta)} \frac{dz}{\sqrt{P(z)}} \quad (25)$$

and (23)

$$f(\phi) \equiv -\frac{1}{2} \arctan [k \tan(\beta(\phi - \phi_0))] = \int_{z_0}^{z(\phi)} \frac{dz}{\sqrt{P(z)}}, \quad (26)$$

such that the general solutions for the radial motion in dependence on the angular variables read

$$r(\theta) = \frac{2m}{\wp(g(\theta) - c) + \frac{1}{3}}, \quad r(\phi) = \frac{2m}{\wp(f(\phi) - c) + \frac{1}{3}} \quad (27)$$

where \wp is the Weierstrass elliptic function and $g(\theta)$ and $f(\phi)$ are the functions appearing in (25) and (26), respectively. Our choice of θ_0 depends on whether the orbit has finite maximal radius or whether it extends to infinity. For orbits with a finite maximal radius, we find it convenient to choose $\theta_0 = \pi - \arcsin(1/k)$ such that

$$g(\theta) \equiv g_1(\theta) = \frac{1}{2} \left[\arcsin \left(\frac{\cos \theta}{\sqrt{1 - k^{-2}}} \right) + \frac{\pi}{2} \right], \quad (28)$$

while for orbits that extend to infinity we choose $\theta_0 = \pi/2$ such that

$$g(\theta) \equiv g_2(\theta) = \frac{1}{2} \arcsin \left(\frac{\cos \theta}{\sqrt{1 - k^{-2}}} \right). \quad (29)$$

In addition we choose $\phi_0 = 0$ for all cases such that from here on

$$f(\phi) = -\frac{1}{2} \arctan [k \tan(\beta\phi)]. \quad (30)$$

The constant c in (27) is given by $c = \int_{z_0}^{\infty} \frac{dz}{\sqrt{4z^3 - g_2z - g_3}}$. For $D \leq 0$ we can always choose $c = 0$. For $D > 0$ we choose $c = 0$ for $z_0 = \infty$, $c = \omega_1$ for $z_0 = e_1$, $c = \omega_1 + \omega_2$ for $z_0 = e_2$ and $c = \omega_2$ for $z_0 = z_3$. Here

$$\omega_1 = \frac{K(K)}{\sqrt{e_1 - e_3}}, \quad \omega_2 = i \frac{K(K')}{\sqrt{e_1 - e_3}}, \quad (31)$$

where K denotes the complete elliptic integral of the first kind and \mathcal{K} is the modulus of the elliptic integral with

$$\mathcal{K} = \sqrt{\frac{e_2 - e_3}{e_1 - e_3}}. \quad (32)$$

Moreover we have $\mathcal{K}' = \sqrt{1 - \mathcal{K}^2}$. For $D > 0$, $D = 0$ and $D < 0$ there are various replacements of the Weierstrass function \wp by real valued Jacobi elliptic functions [18].

In the following, we will discuss different type of orbits, which we denote as follows :

1. Bound orbit : an orbit for which r varies between two finite values.
2. Spherical orbit : a special bound orbit for which r is constant.
3. Bound terminating orbit : a bound orbit that ends at the singularity $r = 0$.
4. Unbound terminating orbit : an orbit for which r varies between $r = 0$ and infinity.
5. Escape orbit : the orbit comes from infinity, approaches a finite r and goes again to $r = \infty$.

A. Geodesics for $D > 0$ and $E^2 - \varepsilon > 0$

This case corresponds to the choice $V_{\text{eff}}^{\min} < \frac{E^2 - \varepsilon}{2} < V_{\text{eff}}^{\max}$ and $E^2 - \varepsilon > 0$ (region I in the λ - μ -plot). The effective potential and the corresponding characteristic polynomial $P(z)$ are shown in Fig.2. The line $\frac{E^2 - \varepsilon}{2}$ intersects the effective potential $V_{\text{eff}}(r)$ twice. The polynomial $P(z)$ has in fact three real zeros e_1, e_2, e_3 . However, for $e_2 < z < e_3$ we have $P(z) < 0$ and in addition $e_1 < -1/3$. We are hence allowed to integrate from e_2 to $z = -1/3$, which corresponds to integration from $r = r_2$ to $r = \infty$ and from e_3 to $z = \infty$ which corresponds to integration from $r = 0$ to $r = r_3$.

1. Escape orbit and light deflection

The range of allowed values for r is indicated by the red horizontal line in Fig.2 and is $r_2 \leq r \leq \infty$.

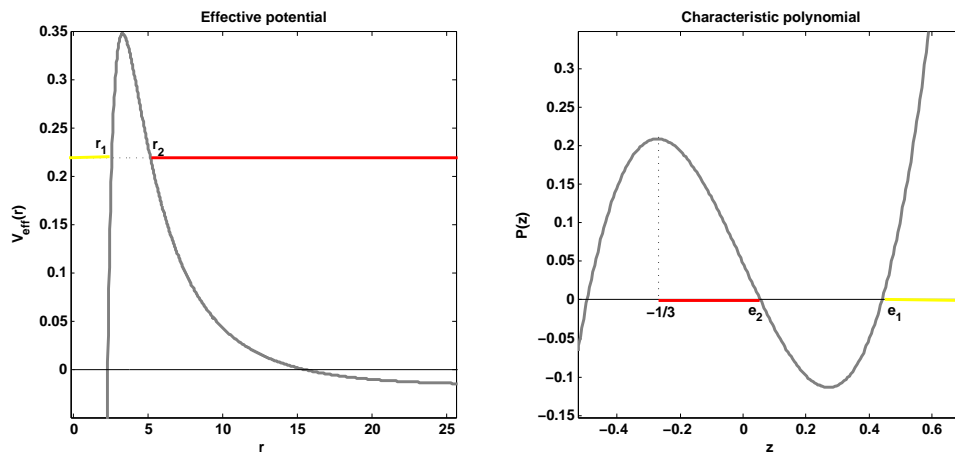


FIG. 2: The effective potential $V_{\text{eff}}(r)$ (left) and the characteristic polynomial $P(z)$ (right) of a massive test particle $\varepsilon = 1$ for $D > 0$. The red horizontal line corresponds to the range of r values for an escape orbit.

The plots of escape orbits of a massive test particle and a massless test particle are given in Fig.3 and Fig.4, respectively. Obviously, for β close to one, test particles get simply deflected. However, if β is significantly smaller than one, particles will approach the minimal radius r_2 , then whirl the black hole and finally move off to infinity again. This is particularly important for the deflection of light.

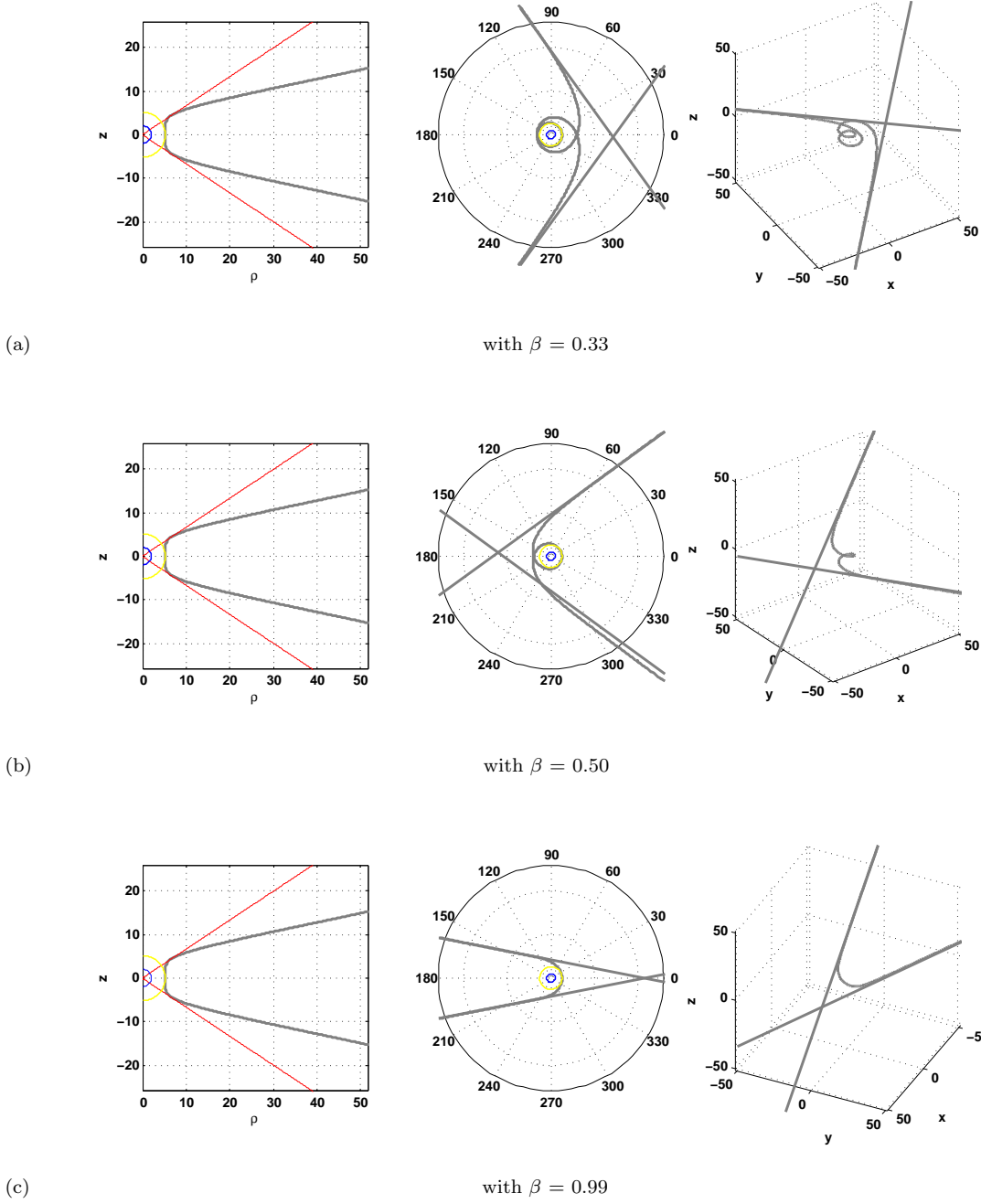


FIG. 3: We show an escape orbit for a massive test particle ($\varepsilon = 1$) in the ρ - z -plane (with $\rho = r \sin \theta$, $z = r \cos \theta$) (left), in the plane perpendicular to \vec{L} (middle) and in \mathbb{R}^3 (right). (a), (b) and (c) correspond to $\beta = 0.33$, $\beta = 0.5$ and $\beta = 0.99$, respectively. Here, we have chosen $E = 1.2$, $L_z = 5$, $k = 1.2$ and $m = 1$. The yellow circles in the ρ - z -plane and in the plane perpendicular to \vec{L} correspond to circles with radius r_2 , respectively.

In order to see the effect of β on the deflection of light ($\varepsilon = 0$) we set $k = 1$ (i.e. we choose $\theta = \pi/2$) and select the initial point at $r_0 = r_2$. The requirement $r(\phi) = \infty$ imposes a bound on ϕ which reads:

$$|\phi| \leq \frac{2}{\beta} \left[\frac{1}{\sqrt{e_1 - e_3}} \int_0^{\varphi_c} \frac{d\varphi}{\sqrt{1 - \mathcal{K}^2 \sin^2(\varphi)}} + \omega_1 \right]. \quad (33)$$

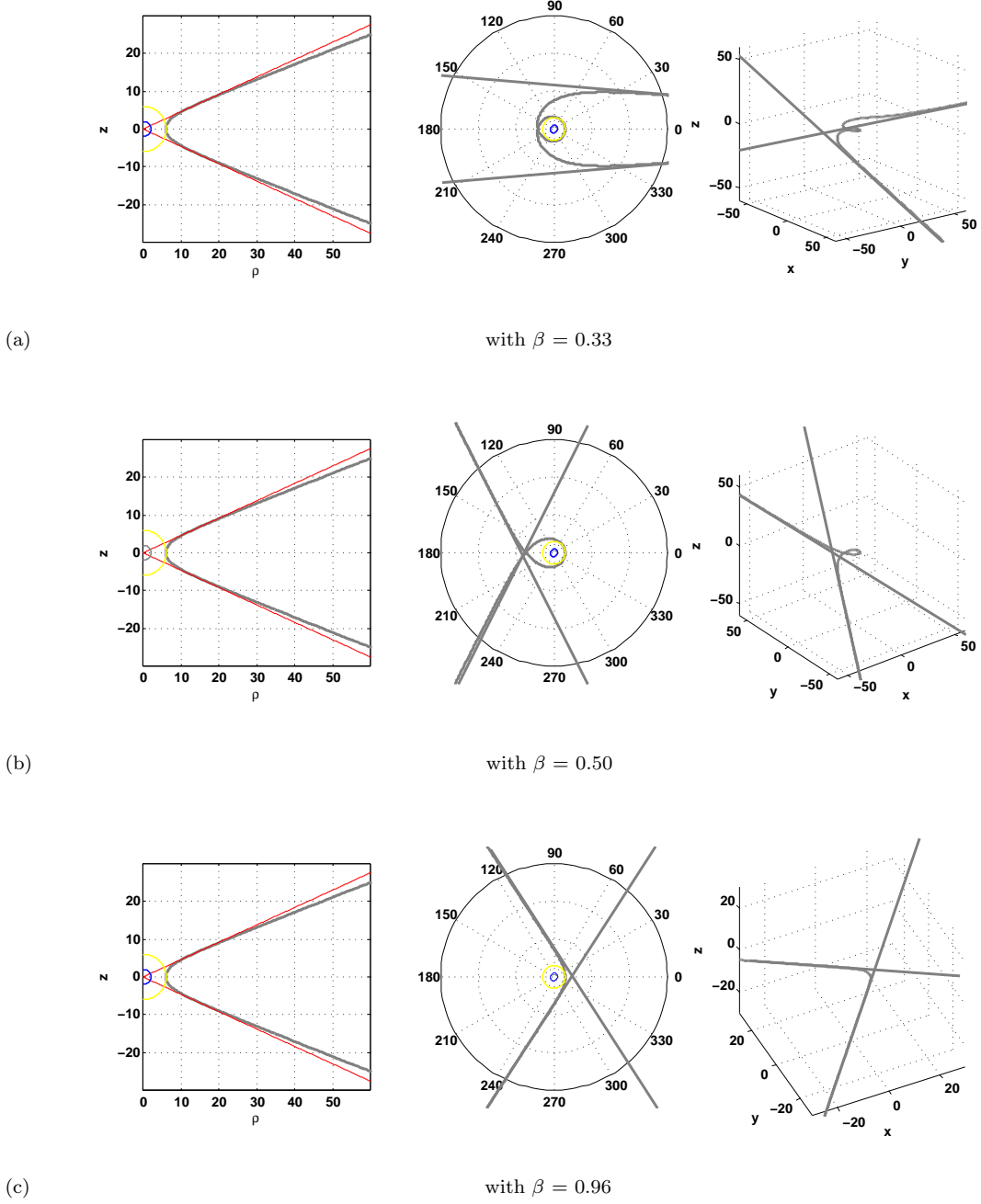


FIG. 4: We show an escape orbit for a massless test particle ($\varepsilon = 0$) in the ρ - z -plane (with $\rho = r \sin \theta$, $z = r \cos \theta$) (left), in the plane perpendicular to \vec{L} (middle) and in \mathbb{R}^3 (right). (a), (b) and (c) correspond to $\beta = 0.33$, $\beta = 0.5$ and $\beta = 0.96$, respectively. Here, we have chosen $E = 0.75$, $L_z = 5$, $k = 1.1$ and $m = 1$. The yellow circles in the ρ - z -plane and in the plane perpendicular to \vec{L} correspond to circles with radius r_2 , respectively.

Therefore the deflection angle $\Delta\phi$ is given by:

$$\Delta\phi = \frac{1}{\beta} \left[\frac{4}{\sqrt{e_1 - e_3}} \int_0^{\varphi_c} \frac{d\varphi}{\sqrt{1 - \mathcal{K}^2 \sin^2(\varphi)}} + 2\omega_1 \right] + \pi \left(\frac{1}{\beta} - 1 \right). \quad (34)$$

The term in the square bracket of (34) is the expression of $\Delta\phi$ for the “pure” Schwarzschild case, i.e. $\beta = 1$ and the

second term takes care of the fact that the space-time has a conical deficit.

Using the parametrized Post-Newtonian (PPN) formalism [20], which describes deviations from standard General Relativity, the angle of light deflection can be given by $\Delta\phi = \frac{1}{2}(1 + \gamma_1)1.75'' = \frac{1}{2}(1 + \gamma_1)(\Delta\phi)_S$ assuming that the parameter γ_1 is equal to unity for General Relativity. $(\Delta\phi)_S$ denotes the General Relativity value assuming the exterior space-time of the massive body to be given by the Schwarzschild solution. Different experimental tests [21–23] have given a value of $\gamma_1 - 1 = (2.1 \pm 2.3) \cdot 10^{-5}$, hence $\frac{\Delta\phi - (\Delta\phi)_S}{(\Delta\phi)_S} \lesssim 10^{-5}$. If we now assume that the deviations of $\Delta\phi$ from the Schwarzschild value are not due to a modification of General Relativity, but due to the presence of a cosmic string, we can approximate the energy per unit length of the cosmic string. Reinstalling factors of c^2 we then find $(1 - \beta) \lesssim 10^{-11}$ which for the deficit angle gives $\Delta \lesssim 10^{-10}$. This transfers to a bound on the energy per unit length given by : $\mu \lesssim 10^{16} \frac{\text{kg}}{\text{m}}$.

2. Bound terminating orbit

The range of allowed r values is indicated in Fig.2 and is $0 \leq r \leq r_1$. We don't discuss this case in detail here, because it is qualitatively similar to the case with $D > 0$ and $E^2 - \varepsilon < 0$ (see discussion below).

B. Geodesics for $D > 0$ and $\frac{E^2 - \varepsilon}{2} < 0$

This case corresponds to the choice $V_{\text{eff}}^{\min} < \frac{E^2 - \varepsilon}{2} < V_{\text{eff}}^{\max}$ and $E^2 - \varepsilon < 0$ (region II in the λ - μ -plot). The effective potential and the corresponding characteristic polynomial $P(z)$ are shown in Fig. 5. The line $\frac{E^2 - \varepsilon}{2}$ intersects the effective potential $V_{\text{eff}}(r)$ three times at r_1 , r_2 and r_3 . These intersection points correspond to the zeros of the characteristic polynomial, which we denote by e_1 , e_2 and e_3 . Apparently, we are allowed to integrate between ∞ and e_1 , which corresponds to integration from $r = 0$ to $r = r_1$, and from e_2 to e_3 , which corresponds to integration from $r = r_2$ to $r = r_3$.

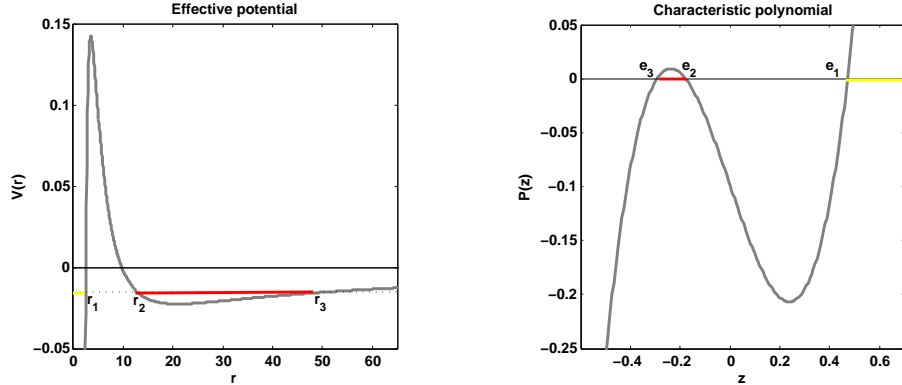


FIG. 5: The effective potential $V_{\text{eff}}(r)$ (left) and the characteristic polynomial $P(z)$ (right) of a massive test particle $\varepsilon = 1$ for $D > 0$. The red horizontal line corresponds to the range of r values for a bound orbit, while the yellow line corresponds to the range of r for a bound terminating orbit.

1. Bound terminating orbit

The range of allowed r values is indicated by the yellow line in Fig.5 and is $0 \leq r \leq r_1$.

A plot of a bound terminating orbit for a massive test particle is given in Fig. 6. We emphasize on the deformation of the orbits when changing the deficit parameter β . While for $\beta = 0.99$, the orbit is still nearly planar, this changes with the decrease of β , i.e. the increase of the deficit angle. While the orbit looks heart-shaped for $\beta = 0.99$, the increase of the deficit angle leads to a pretzel-like structure.

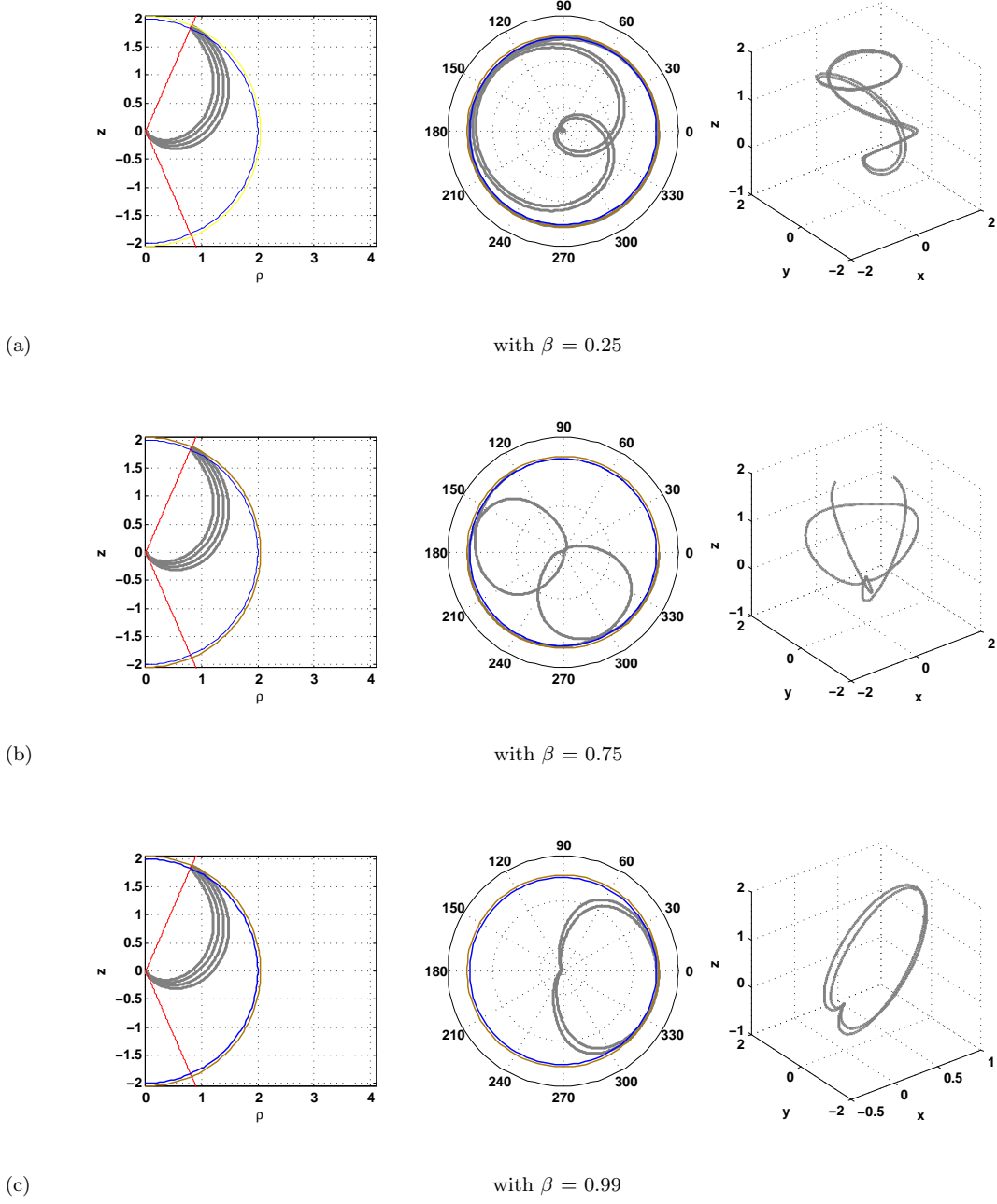


FIG. 6: We show a bound terminating orbit for a massive test particle ($\varepsilon = 1$) in the ρ - z -plane (with $\rho = r \sin \theta$, $z = r \cos \theta$) (left), in the x - y -plane (middle) and in \mathbb{R}^3 (right). (a), (b) and (c) correspond to $\beta = 0.25$, $\beta = 0.75$ and $\beta = 0.99$, respectively. Here, we have chosen $E = 0.9975$, $L_z = 5$, $k = 2.5$ and $m = 1$. The blue and the dark yellow circles in the ρ - z -plane and in the x - y -plane correspond to circles with Schwarzschild radius $r_s = 2m = 2$ and maximal radius r_1 , respectively.

2. Bound orbit and perihelion shift

The range of allowed r -values is indicated by the red line in Fig.5 and is $r_2 \leq r \leq r_3$.

A bound orbit of a massive test particle is given in Fig. 7 for different choices of β . For β close to one, the orbit corresponds to a standard closed orbit, while decreasing β leads to the appearance of additional loops in the orbit (see the cases $\beta = 0.25$ and $\beta = 0.75$). This is important in order to understand the perihelion shift of test particles orbiting a massive body that is pierced by a cosmic string.

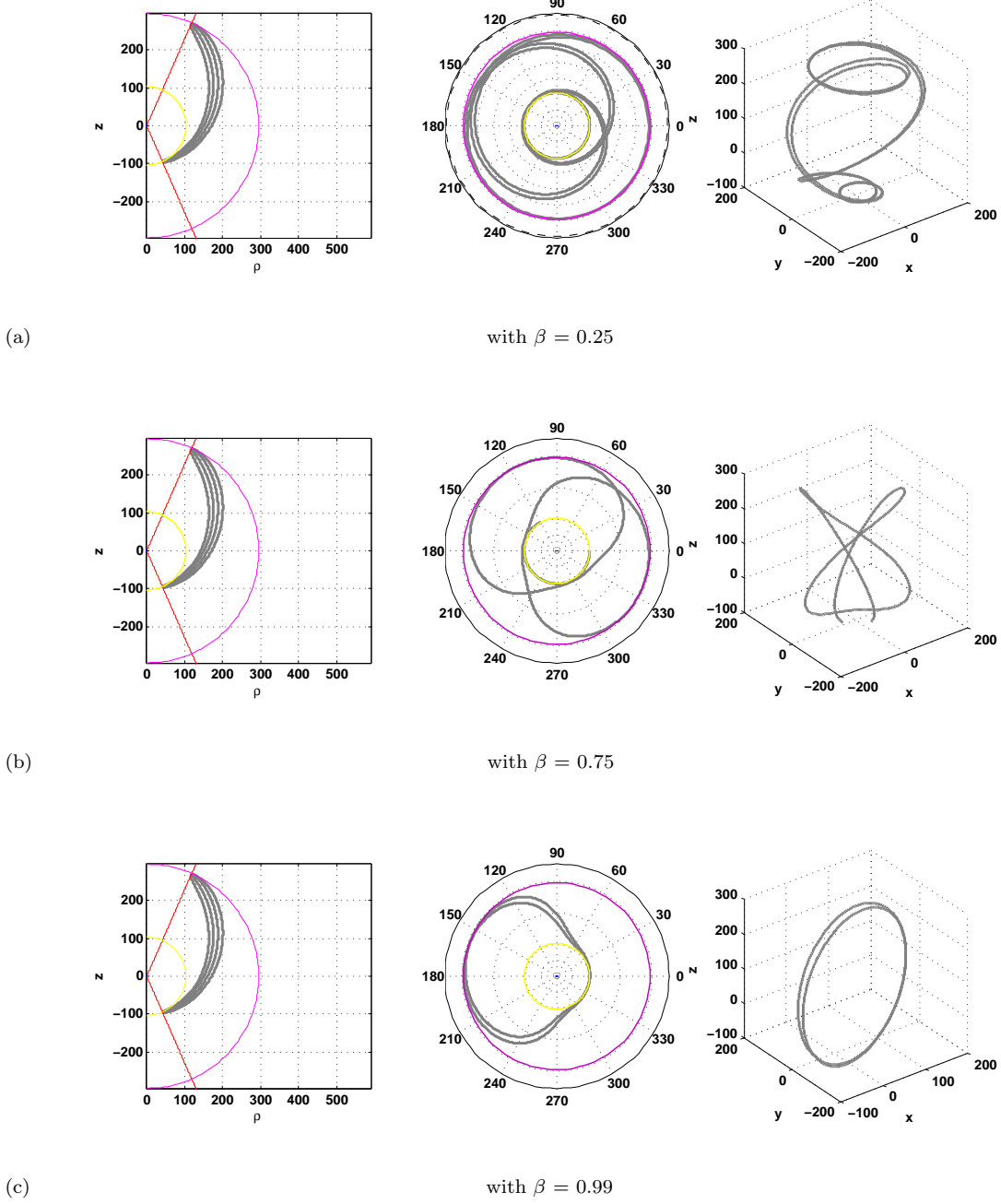


FIG. 7: We show a bound orbit for a massive test particle ($\varepsilon = 1$) in the ρ - z -plane (with $\rho = r \sin \theta$, $z = r \cos \theta$) (left), in the plane perpendicular to \vec{L} (middle) and in \mathbb{R}^3 (right). (a), (b) and (c) correspond to $\beta = 0.25$, $\beta = 0.75$ and $\beta = 0.99$, respectively. Here, we have chosen $E = 0.9975$, $L_z = 5$, $k = 2.5$ and $m = 1$. The yellow and magenta circles in the ρ - z -plane and in the plane perpendicular to \vec{L} correspond to circles with radius r_2 and maximal radius r_3 , respectively.

For bound orbits the perihelion shift depends on the deficit parameter β . This effect has been calculated approximately in [14]. Here, we will give the exact analytic formula for the perihelion shift. We choose $k = 1$ in order to study planar orbits with $\theta = \pi/2$. We then have for the motion in the plane:

$$r(\phi) = \frac{2m}{\wp(\frac{\beta\phi}{2}) + \frac{1}{3}}. \quad (35)$$

When the test particle moves from $r_3 \rightarrow r_2 \rightarrow r_3$ we find for the change in ϕ :

$$\delta\phi = \frac{4}{\beta} \frac{K(\mathcal{K})}{\sqrt{e_1 - e_3}} \quad (36)$$

such that the perihelion shift $\Delta\phi$ reads

$$\Delta\phi = \delta\phi - 2\pi = \frac{4}{\beta} \frac{K(\mathcal{K})}{\sqrt{e_1 - e_3}} - 2\pi. \quad (37)$$

In Fig.8, we plot the value of $\Delta\phi$ in dependence on β for $m = 1$, $L_z = 5$, $k = 1$ and $E = 0.999$. Obviously, the perihelion shift can become quite large due to the conical nature of the space-time. Perihelion shifts in the solar system are quite small and the level of agreement of the measured value with that predicted by assuming the gravitational field of the sun to be described by the Schwarzschild solution can be used to give an upper bound on the energy density per unit length of a cosmic string present in the solar system. However, a large perihelion shift of 39° per orbit has been observed in a massive binary black hole system [19]. Note that if we would do a similar approximation as that done in [14], we would find

$$\Delta\phi = \frac{1}{\beta}(\Delta\phi)_S + 2\pi \left(\frac{1}{\beta} - 1 \right), \quad (38)$$

where $(\Delta\phi)_S$ denotes the perihelion shift in the Schwarzschild case $\beta = 1$. Within the PPN formalism [20], the perihelion shift can be written as $\Delta\phi = 42.98'' \left(\frac{1}{3}(2 + 2\gamma_1 - \gamma_2) \right)$ assuming that the parameters γ_1 and γ_2 are equal to unity for General Relativity and that the quadrupole moment of the sun vanishes. Different experimental tests [21–23] have given $\gamma_2 - 1 = (1.2 \pm 1.1) \cdot 10^{-4}$, hence $\frac{\Delta\phi - (\Delta\phi)_S}{(\Delta\phi)_S} \lesssim 10^{-4}$.

If we now assume that the deviations of $\Delta\phi$ from the Schwarzschild value are not due to a modification of General Relativity, but due to the presence of a cosmic string, we can approximate the energy per unit length of the cosmic string. Again reinstalling factors of c^2 we find $(1 - \beta) \lesssim 10^{-10}$ which for the deficit angle gives $\Delta \lesssim 10^{-9}$. This transfers to a bound on the energy per unit length which is given by : $\mu \lesssim 10^{17} \frac{\text{kg}}{\text{m}}$.

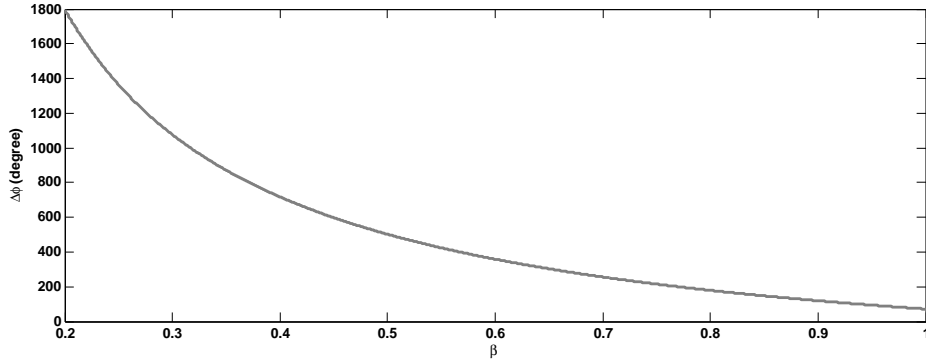


FIG. 8: The perihelion shift $\Delta\phi$ in dependence on the deficit parameter β for $m = 1$, $L_z = 5$, $k = 1$ and $E = 0.999$.

C. Geodesics for $D < 0$ and $E^2 - \frac{2}{3}\varepsilon > \frac{L^2}{54m^2}$

This case corresponds to the choice $V_{\text{eff}}^{\text{max}} < \frac{E^2 - \varepsilon}{2}$ (region III in the λ - μ -plot). The effective potential and the corresponding characteristic polynomial $P(z)$ are shown in Fig. 9. The line $\frac{E^2 - \varepsilon}{2}$ does not intersect the effective potential $V_{\text{eff}}(r)$. The polynomial $P(z)$ has a single real zero at e_1 , however $e_1 < -1/3$. We are allowed to integrate between $z = \infty$ and $z = -1/3$, which corresponds to integration from $r = 0$ to $r = \infty$.

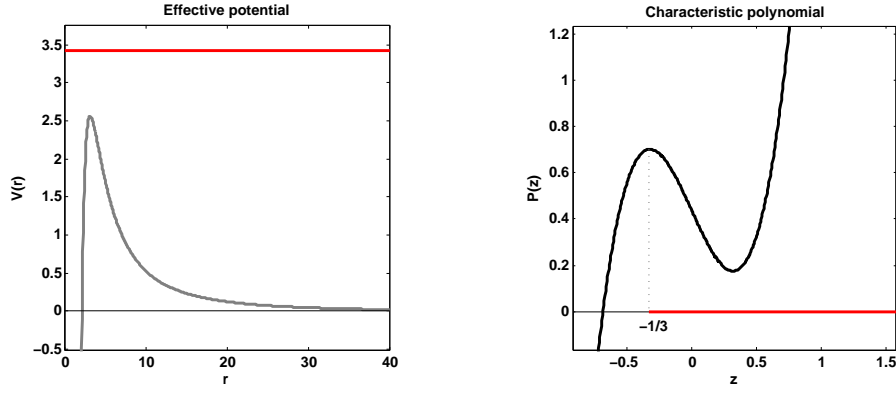


FIG. 9: The effective potential $V_{\text{eff}}(r)$ (left) and the characteristic polynomial $P(z)$ (right) for $D < 0$ and $E^2 - \frac{2}{3}\varepsilon > \frac{L^2}{54m^2}$. The red horizontal line corresponds to the range of r values for an escape orbit.

1. Escape orbit

The range of allowed r values is indicated by the red horizontal line in Fig.9 and corresponds to $0 \leq r \leq \infty$. The plot of an escape orbit in this case is shown in Fig.10. The particle comes in from infinity and – after a few loops – ends in $r = 0$.

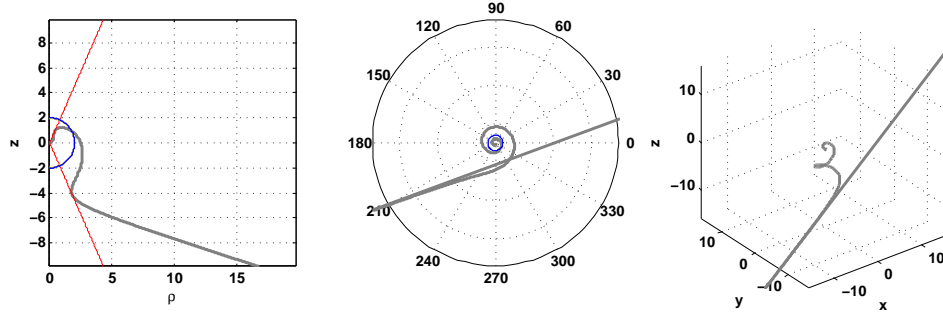


FIG. 10: We show a bound terminating orbit for a massive test particle ($\varepsilon = 1$) in the ρ - z -plane (with $\rho = r \sin \theta$, $z = r \cos \theta$) (left), in the plane perpendicular to \vec{L} (middle) and in \mathbb{R}^3 (right). Here, we have chosen $\beta = 0.4$, $E = 2.8$, $L_z = 5$, $k = 2.5$ and $m = 1$. The blue circles in the ρ - z -plane and in the plane perpendicular to \vec{L} correspond to circles with Schwarzschild radius $r_s = 2m = 2$.

D. Geodesics for $D < 0$ and $E^2 - \frac{2}{3}\varepsilon < \frac{L^2}{54m^2}$

This case corresponds to the choice $V_{\text{eff}}^{\min} > \frac{E^2 - \varepsilon}{2}$ (region IV in the λ - μ -plot). The effective potential and the corresponding characteristic polynomial $P(z)$ are shown in Fig. 11. The line $\frac{E^2 - \varepsilon}{2}$ intersects the effective potential $V_{\text{eff}}(r)$ only once at r_1 . This intersection point corresponds to the single real zero of the characteristic polynomial, which we denote by e_1 . Apparently, we are allowed to integrate between ∞ and e_1 , which corresponds to integration from $r = 0$ to $r = r_1$.

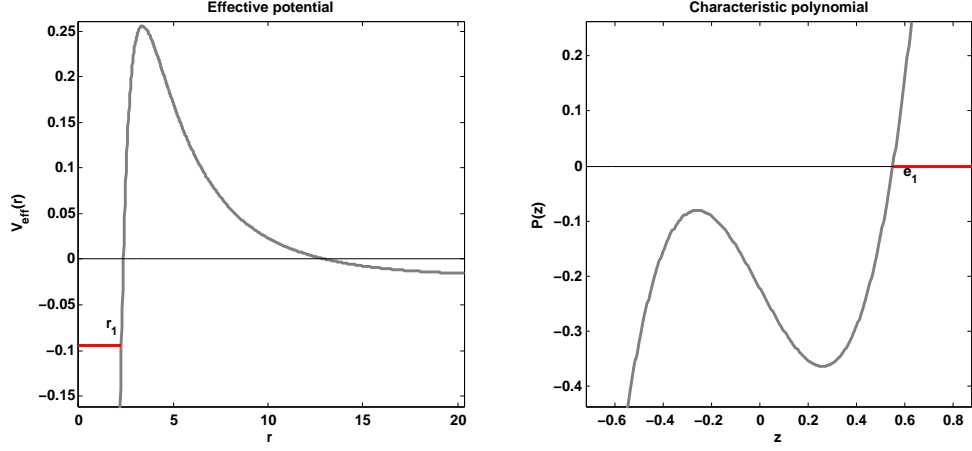


FIG. 11: The effective potential $V_{\text{eff}}(r)$ (left) and the characteristic polynomial $P(z)$ (right) for $D < 0$ and $E^2 - \frac{2}{3}\varepsilon < \frac{L^2}{54m^2}$. The red horizontal line corresponds to the range of r values for a bound terminating orbit.

1. Bound terminating orbits

The range of allowed r values is indicated by the red line in Fig.11 and is $0 \leq r \leq r_1$.

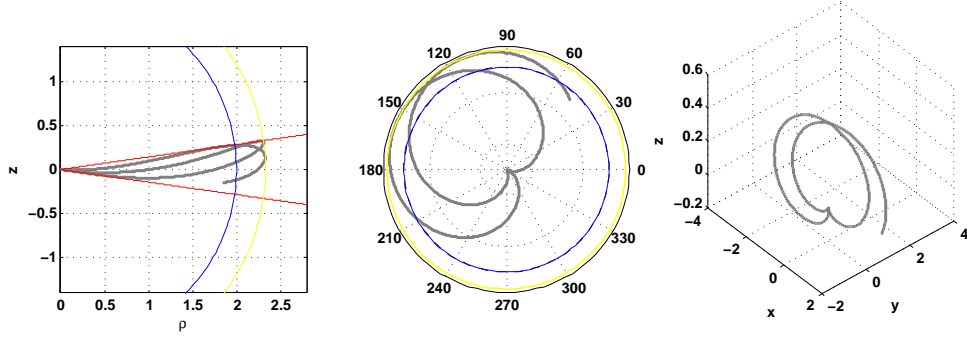


FIG. 12: We show a bound terminating orbit for a massive test particle ($\varepsilon = 1$) in the ρ - z -plane (with $\rho = r \sin \theta$, $z = r \cos \theta$) (left), in the plane perpendicular to \vec{L} (middle) and in \mathbb{R}^3 (right). Here, we have chosen $\beta = 0.99$, $E = 0.9$, $L_z = 5$, $1/k = 0.99$ and $m = 1$. The dark yellow and blue circles in the ρ - z -plane and in the plane perpendicular to \vec{L} correspond to circles with radius r_1 and Schwarzschild radius $r_s = 2m = 2$, respectively.

The example of a bound terminating orbit for a massive test particle for $\beta = 0.99$ is given in Fig.12.

E. Geodesics for $D = 0$ and $E^2 - \varepsilon > 0$

This case corresponds to the choice $V_{\text{eff}}^{\text{max}} = \frac{E^2 - \varepsilon}{2} > 0$. The effective potential and the corresponding characteristic polynomial $P(z)$ are shown in Fig. 13. The line $\frac{E^2 - \varepsilon}{2}$ intersects the effective potential $V_{\text{eff}}(r)$ only once at $r_1 = r_2$, i.e. at the maximum of the effective potential. This intersection point corresponds to a double zero of the characteristic polynomial, which we denote by $e_1 = e_2$. Apparently, we are allowed to integrate between ∞ and e_1 , which corresponds to integration from $r = 0$ to $r = r_1$ and from e_1 to $z = -1/3$, which corresponds to integration from $r = r_1$ to $r = \infty$.

Note that the spherical orbit with $r = r_1 = r_2 = \text{const.}$ corresponds to the unstable spherical orbit discussed in [16].

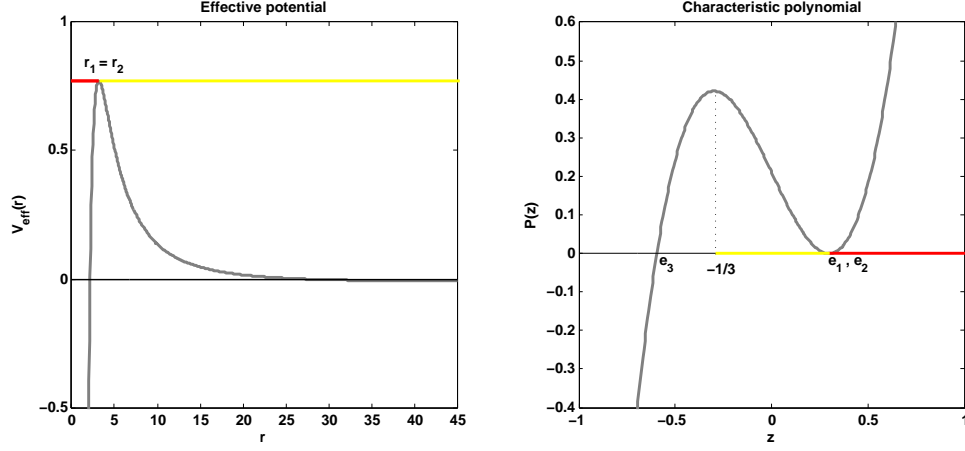


FIG. 13: The effective potential $V_{\text{eff}}(r)$ (left) and the characteristic polynomial $P(z)$ (right) for $D = 0$ and $E^2 - \varepsilon > 0$. The red horizontal line corresponds to the range of r values for a bound terminating orbit, while the yellow line corresponds to the range of r for an unbound terminating orbit.

1. Unbound terminating orbit

The range of allowed r values is indicated by the yellow line in (13) and is $r_1 \leq r \leq \infty$.

An example of an unbound terminating orbit is given in Fig.14 for $\beta = 0.65$. The test particle comes from infinity and approaches an unstable spherical orbit with $r = r_1 = r_2 = \text{const.}$.

2. Bound terminating orbit

In this particular case the effective potential $V_{\text{eff}}(r)$ has its maximum at the maximal radius $r = r_1$ of the orbit. The range of allowed r values is indicated by the red line in (13) and is $0 \leq r \leq r_1$.

An example of a bound terminating orbit is shown in Fig.15 for $\beta = 0.65$. The particle starts at $r = 0$ and approaches the unstable spherical orbit at $r = r_1 = r_2 = \text{const.}$.

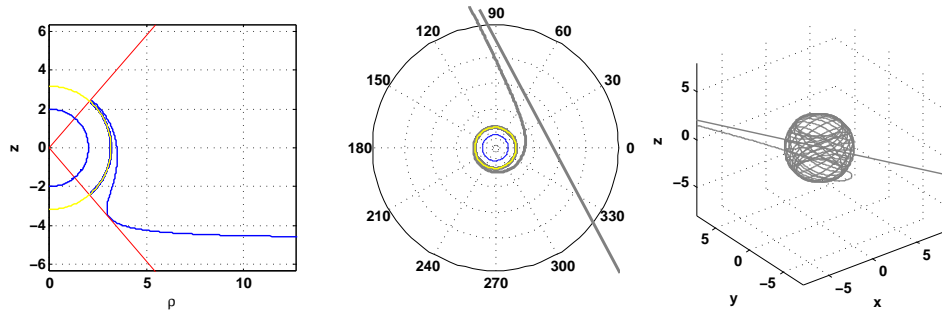


FIG. 14: We show an unbound terminating orbit for a massive test particle ($\varepsilon = 1$) in the ρ - z -plane (with $\rho = r \sin \theta$, $z = r \cos \theta$) (left), in the plane perpendicular to \vec{L} (middle) and in \mathbb{R}^3 (right). We have chosen $\beta = 0.65$, $E = 1.594$, $L_z = 5$, $1/k = 0.65$ and $m = 1$. The dark yellow circles in the ρ - z -plane and in the plane perpendicular to \vec{L} correspond to circles with radius $r_1 = r_2$.

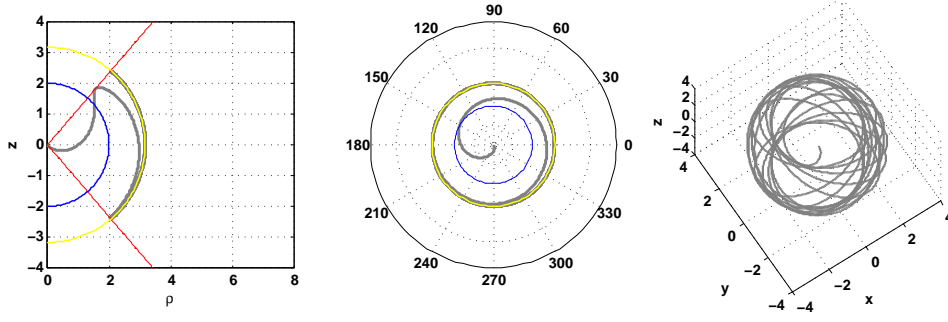


FIG. 15: We show a bound terminating orbit for a massive test particle ($\varepsilon = 1$) in the ρ - z -plane (with $\rho = r \sin \theta$, $z = r \cos \theta$) (left), in the plane perpendicular to \vec{L} (middle) and in \mathbb{R}^3 (right). We have chosen $\beta = 0.65$, $E = 1.594$, $L_z = 5$, $1/k = 0.65$ and $m = 1$. The dark yellow and blue circles in the ρ - z -plane and in the plane perpendicular to \vec{L} correspond to circles with radius r_1 and Schwarzschild radius $r_s = 2m = 2$, respectively.

F. Geodesics for $D = 0$ and $E^2 - \varepsilon < 0$

This case corresponds to the choice $V_{\text{eff}}^{\text{max}} = \frac{E^2 - \varepsilon}{2} < 0$. The effective potential and the corresponding characteristic polynomial $P(z)$ are shown in Fig. 16. The line $\frac{E^2 - \varepsilon}{2}$ intersects the effective potential $V_{\text{eff}}(r)$ at $r_1 = r_2$ and at r_3 . These intersection points correspond to a double zero $e_1 = e_2$ and a simple zero at e_3 . We are only allowed to integrate between $e_1 = e_2$ and e_3 which corresponds to integration between $r_1 = r_2$ and r_3 as well as between $z = \infty$ and e_3 which corresponds to integration between $r = 0$ and $r_1 = r_2$.

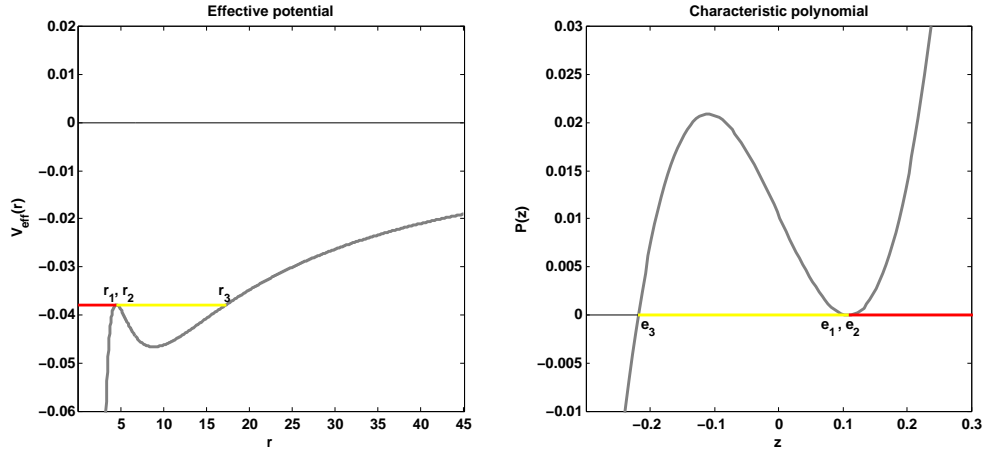


FIG. 16: The effective potential $V_{\text{eff}}(r)$ (left) and the characteristic polynomial $P(z)$ (right) for $D = 0$ and $E^2 - \varepsilon < 0$. The red horizontal line corresponds to the range of r values for a bound terminating orbit, while the yellow line corresponds to the range of r for a bound orbit.

1. Bound orbit

The range of allowed r values is indicated in Fig.16 by the horizontal yellow line and is $r_1 \leq r \leq r_3$.

An example of a bound orbit is given in Fig.17 for $\beta = 0.9$. This is an example of a so-called homoclinic orbit. Homoclinic orbits are orbits that approach unstable circular orbits and have been discussed extensively in the context

of gravitational wave production in binary system. There they play the role of a transition between the late inspiral and the final plunge [24].

2. Bound terminating orbit

In this particular case the effective potential has its maximum at the maximal radius $r = r_1$ of the orbit. An example of a bound terminating orbit is given in Fig.18.

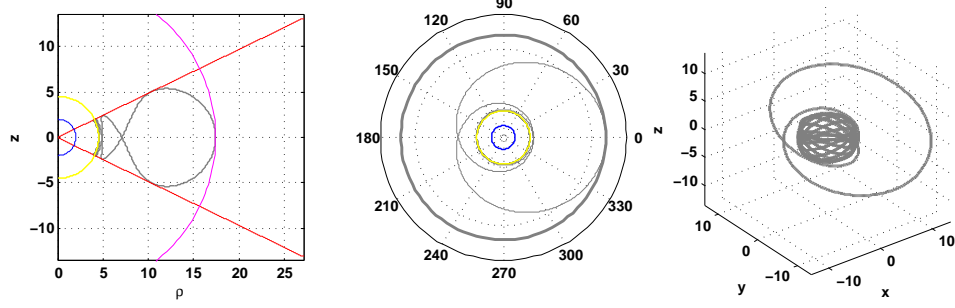


FIG. 17: We show a bound orbit for a massive test particle ($\varepsilon = 1$) in the ρ - z -plane (with $\rho = r \sin \theta$, $z = r \cos \theta$) (left), in the plane perpendicular to \vec{L} (middle) and in \mathbb{R}^3 (right). We have chosen $\beta = 0.9$, $E = 0.9614$, $L_z = 3.3$, $k = \frac{10}{9}$ and $m = 1$. The dark yellow and violet circles in the ρ - z -plane and in the plane perpendicular to \vec{L} correspond to circles with radius r_2 and r_3 , respectively.

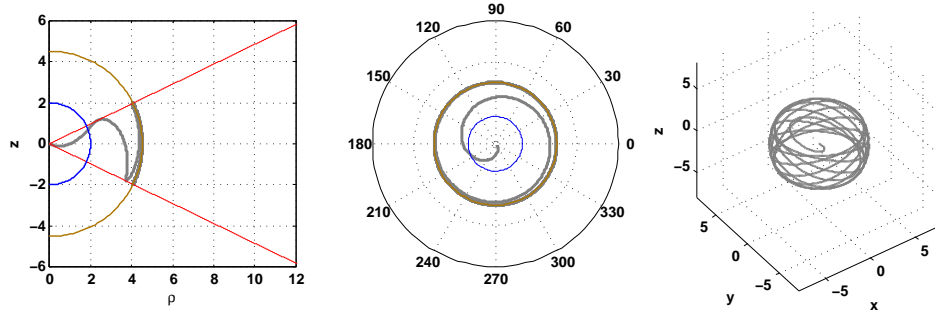


FIG. 18: We show a bound terminating orbit for a massive test particle ($\varepsilon = 1$) in the ρ - z -plane (with $\rho = r \sin \theta$, $z = r \cos \theta$) (left), in the plane perpendicular to \vec{L} (middle) and in \mathbb{R}^3 (right). We have chosen $\beta = 0.9$, $E = 0.9614$, $L_z = 3.3$, $k = \frac{10}{9}$ and $m = 1$. The dark yellow circles in the ρ - z -plane and in the plane perpendicular to \vec{L} correspond to circles with radius r_2 .

G. Geodesics for $D = 0$ and $\frac{E^2}{L^2} = \frac{1}{54m^2}$

This case corresponds to the choice $V_{\text{eff}}^{\min} = \frac{E^2 - \varepsilon}{2}$. The effective potential and the corresponding characteristic polynomial $P(z)$ are shown in Fig. 19. The line $\frac{E^2 - \varepsilon}{2}$ intersects the effective potential $V_{\text{eff}}(r)$ at $r = 6m$. This corresponds to $e_1 = e_2 = e_3 = 0$. We are allowed to integrate from $e_1 = e_2 = e_3$ to $z = \infty$, which corresponds to integration from $r_1 = r_2 = r_3 = 6m$ to $r = \infty$.

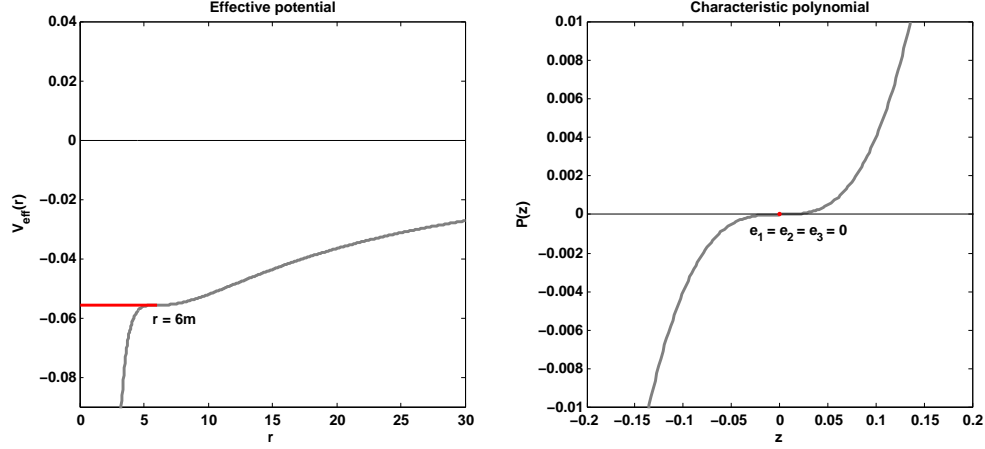


FIG. 19: The effective potential $V_{\text{eff}}(r)$ (left) and the characteristic polynomial $P(z)$ (right) for $D = 0$ and $\frac{E^2}{L^2} = \frac{1}{54m^2}$. The red horizontal line corresponds to the range of r values for a bound terminating orbit.

1. Bound terminating orbit

The range of allowed r values is indicated by the horizontal red line in Fig.19 and is $0 \leq r \leq 6m$. An example of a bound terminating orbit is given in Fig.20 for $\beta = 0.9$.

2. Spherical orbit

For $r_0 = 6m$ we have a spherical orbit. These spherical orbits have already been discussed in [16]. An example of a spherical orbit is given in Fig.21 for $\beta = 0.9$.

H. Geodesics for $D = 0$ and $E^2 - \frac{2}{3}\varepsilon < \frac{L^2}{54m^2}$

The effective potential and the corresponding characteristic polynomial $P(z)$ are shown in Fig. 22. The line $\frac{E^2 - \varepsilon}{2}$ intersects the effective potential $V_{\text{eff}}(r)$ at r_1 and at the minimum of the effective potential at $r = r_2$. These intersection points corresponds to a simple zero e_1 and a double zero at $e_2 = e_3$. We are only allowed to integrate between ∞ and e_1 , which corresponds to integration from $r = 0$ to $r = r_1$.

1. Bound terminating orbit

An example of a bound terminating orbit is shown in Fig.23.

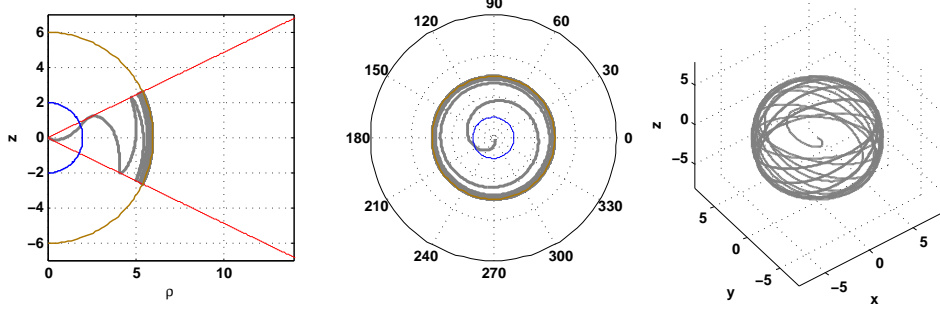


FIG. 20: We show a bound terminating orbit for a massive test particle ($\varepsilon = 1$) in the ρ - z -plane (with $\rho = r \sin \theta$, $z = r \cos \theta$) (left), in the plane perpendicular to \vec{L} (middle) and in \mathbb{R}^3 (right). We have chosen $\beta = 0.9$, $E = \sqrt{8/9}$, $L_z = \sqrt{12 \times (0.9)^2}$, $k = \frac{10}{9}$ and $m = 1$. The dark yellow and blue circles in the ρ - z -plane and in the plane perpendicular to \vec{L} correspond to circles with radius $r = 6m = 6$ and the Schwarzschild radius $r_s = 2m = 2$, respectively.

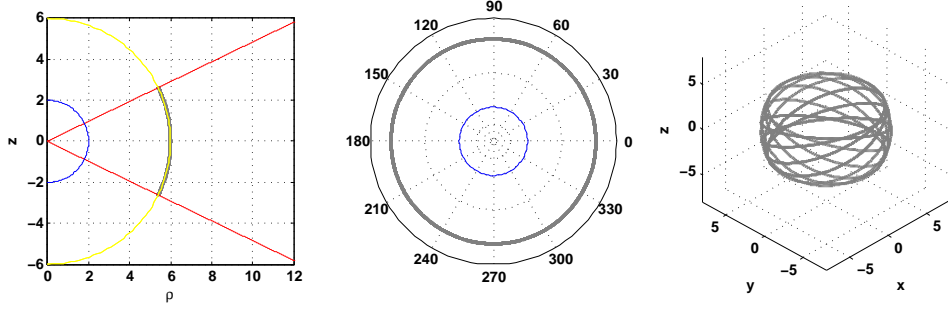


FIG. 21: We show a spherical orbit for a massive test particle ($\varepsilon = 1$) in the ρ - z -plane (with $\rho = r \sin \theta$, $z = r \cos \theta$) (left), in the plane perpendicular to \vec{L} (middle) and in \mathbb{R}^3 (right). We have chosen $\beta = 0.9$, $E = \sqrt{8/9}$, $L_z = \sqrt{12 \times (0.9)^2}$, $k = \frac{10}{9}$ and $m = 1$. The dark yellow and blue circles in the ρ - z -plane and in the plane perpendicular to \vec{L} correspond to circles with radius $r = 6m = 6$ and the Schwarzschild radius $r_s = 2m = 2$, respectively.

2. Spherical orbit

Choosing $r_0 = r_2$ we find a spherical orbit with radius r_2 . In this case, the spherical orbit is a stable spherical orbit. The qualitative plot is similar to the plot given in Fig.21.

IV. NEWTONIAN LIMIT

Assuming the gravitational field to be weak and the test particles to move slowly, we can give the Newtonian limit of our equations. This reads [26]:

$$\frac{d\vec{r}^2}{dt^2} = \frac{1}{2} \vec{\nabla} h_{00} \quad (39)$$

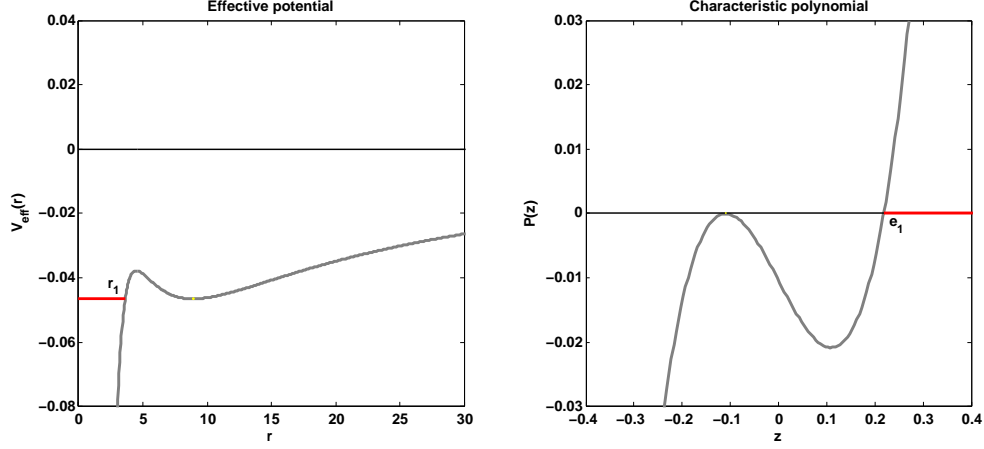


FIG. 22: The effective potential $V_{\text{eff}}(r)$ (left) and the characteristic polynomial $P(z)$ (right) for $D = 0$ and $E^2 - \frac{2}{3}\varepsilon < \frac{L^2}{54m^2}$. The red horizontal line corresponds to the range of r values for a bound terminating orbit.

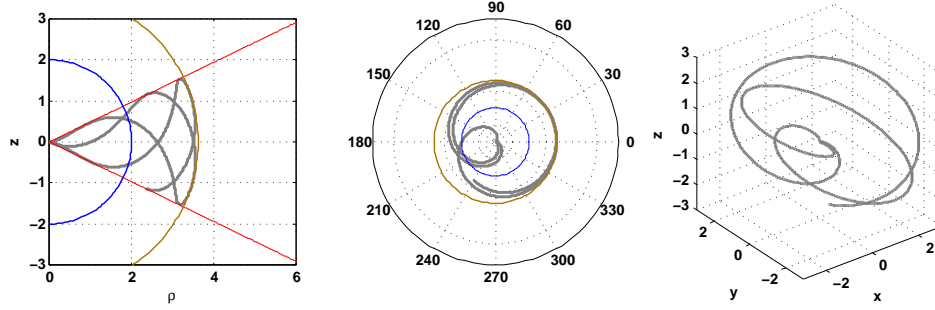


FIG. 23: We show a bound terminating orbit for a massive test particle ($\varepsilon = 1$) in the ρ - z -plane (with $\rho = r \sin \theta$, $z = r \cos \theta$) (left), in the plane perpendicular to \vec{L} (middle) and in \mathbb{R}^3 (right). We have chosen $\beta = 0.9$, $E = 0.95229$, $L_z = 3.3$ and $k = \frac{10}{9}$.

where we assume $g_{\mu\nu} = \eta_{\mu\nu} + h_{\mu\nu}$ with $h_{\mu\nu}$ very small and $\eta_{\mu\nu}$ to be the Minkowski metric. Proceeding as in classical mechanics, we find the Virial theorem

$$-2 \langle T \rangle = \frac{1}{2} \langle \vec{r} \cdot \vec{\nabla} h_{00} \rangle = \frac{1}{2} \langle r \partial_r h_{00} \rangle \quad (40)$$

where $\langle .. \rangle$ denotes the temporal average and $T = \frac{1}{2} \left(\frac{d\vec{r}}{dt} \right)^2$ is the kinetic energy. Hence, the Virial theorem doesn't change for $\beta \neq 1$ as compared to the Newtonian limit of the standard Schwarzschild case $\beta = 1$. However, note that the kinetic energy T has a β -dependence since

$$\left(\frac{d\vec{r}}{dt} \right)^2 = \left(\frac{dr}{dt} \right)^2 + r^2 \left(\frac{d\theta}{dt} \right)^2 + r^2 \sin^2 \theta \beta^2 \left(\frac{d\phi}{dt} \right)^2. \quad (41)$$

Since the average of the potential energy $\langle r \partial_r h_{00} \rangle$ does not depend on β and the Virial theorem holds for all β this means that when $\beta < 1$ the angular velocity $\left(\frac{d\phi}{dt} \right)^2$ increases. We have – in fact – seen this effect when studying the perihelion shift of planets. For the same interval of eigentime, the planet moves further in a space-time with $\beta < 1$ as compared to in a space-time with $\beta = 1$.

In addition, it is easy to show that Kepler's third law $T^2/a^3 = \text{const.}$, where T is the period of the orbit and a the semimajor axis also doesn't change. This is easiest to see when considering circular and planar orbits with $L_z = L$,

i.e. $\theta = \pi/2$. For these, we let $\dot{r} = 0$ and substitute L_z/r from $\dot{\phi}$ into \dot{r} (see (11) and (12)). After separation the two sides can be integrated to give the period of the orbit. The relation will contain a dependence on β . However, note that the integration in ϕ is from 0 to $2\pi\beta$ such that the β cancels and T and a are independent of β .

V. CONCLUSIONS AND OUTLOOK

In this paper, we have constructed the complete set of geodesics in the space-time of a Schwarzschild black hole pierced by a cosmic string. We have classified the geodesics according to their energy, angular momentum aligned with the axis of the string L_z , the ratio between total angular momentum and L_z , the horizon radius of the black hole and the deficit angle (or energy per unit length of the string). We found that the change of the deficit angle doesn't effect the $r(\theta)$ motion, but that the $r(\phi)$ motion changes significantly. Moreover, the motion of the particles is in general not planar. We found a bound of the energy per unit length of the string comparing our results with experimental tests of General Relativity. From perihelion shift and light deflection we found $\mu \lesssim 10^{17} \frac{\text{kg}}{\text{m}}$ and $\mu \lesssim 10^{16} \frac{\text{kg}}{\text{m}}$, respectively. The existence of cosmic strings may also influence the creation of gravitational waves since for inspirals and flybys the deficit angle modifies the angular velocity and, thus, the temporal change of the effective quadrupole responsible for the emitted gravitational wave. The results obtained in this paper can be generalized to rotating black holes, i.e. to the space-time of a Kerr black hole pierced by a cosmic string. They can further be generalized to a Schwarzschild-de Sitter black hole pierced by a cosmic string. For treating such orbits one has to apply hyperelliptic integration developed in [3]. We expect the same enlarged variety of orbits as we encountered in Schwarzschild-de Sitter space-time as compared to Schwarzschild space-time.

Acknowledgements We thank the DFG and Jacobs University Bremen for financial support. We also thank A. Aliev for bringing reference [15] to our attention.

-
- [1] Y. Hagihara, *Theory of relativistic trajectories in a gravitational field of Schwarzschild*, Japan. J. Astron. Geophys. **8**, 67 (1931).
 - [2] S.Chandrasekhar, *The Mathematical Theory of black holes*, Oxford University Press (1998).
 - [3] E. Hackmann and C. Lämmerzahl, Phys. Rev. D **78** 024035 (2008); Phys. Rev. Lett. **100**, 171101 (2008).
 - [4] E. Hackmann, V. Kagramanova, J. Kunz and C. Lämmerzahl, Phys. Rev. D **78** 124018 (2008); [Erratum-ibid. **79** (2009) 029901]
 - [5] E. Hackmann, V. Kagramanova, J. Kunz and C. Lämmerzahl, *Analytic solutions of the geodesic equation in Kerr-(anti-)de Sitter space-times*, Phys. Rev. D, to appear; E. Hackmann, C. Lämmerzahl, and A. Macias, *Complete classification of geodesic motion in fast Kerr and Kerr-(anti-)de Sitter space-times*, In: *New trends in statistical physics: Festschrift in honour of Leopoldo Garcia-Colin's 80th birthday* (World Scientific, Singapore 2010), to appear.
 - [6] E. Hackmann, V. Kagramanova, J. Kunz and C. Lämmerzahl, Europhys. Lett. **88**, 30008 (2009).
 - [7] see e.g. J. Polchinski, *Introduction to cosmic F- and D-strings*, hep-th/0412244 and reference therein.
 - [8] A. Vilenkin and P. Shellard, *Cosmic strings and other topological defects*, Cambridge University Press (1994).
 - [9] M. Majumdar and A. Davis, JHEP **03**, 056 (2002); S. Sarangi and S. Tye, Phys. Lett.B **536**, 185 (2002).
 - [10] R. Bach and H. Weyl, Math. Zeit. **13**, 134 (1922).
 - [11] M. Aryal, L. Ford and A. Vilenkin, Phys. Rev. D **34**, 2263 (1986)
 - [12] F. Dowker, R. Gregory and J. Traschen, Phys. Rev. D **45**, 2762 (1992).
 - [13] A. Achúcarro, R. Gregory and K. Kuijken, Phys. Rev. D **52**, 5729 (1995).
 - [14] W. Freire, V. Bezerra and J. Lima, Gen. Rel. Grav. **33** 1407 (2001).
 - [15] A. Aliev and D. Gal'tsov, Piz'ma Astron. Zh. **14**, 116 (1988); *translated in* Sov. Astron. Lett. **14**, 48 (1988).
 - [16] D. Gal'tsov and E. Masar, Class. Quantum Grav. **6**, 1313 (1989).
 - [17] S. Chakraborty and L. Biswas, Class. Quantum Grav. **13**, 2153 (1996).
 - [18] M. Abramowitz, I. A. Stegun, 1972. Handbook of Mathematical Functions with Formulas, Graphs, and Mathematical Tables, 9th printing. New York: Dover, pp. 627-671.
 - [19] M. J. Valtonen et. al, Nature **452**, 851 (2008).
 - [20] see e.g. C. Will, *Theory and Experiment in Gravitational physics*, Cambridge University Press (1993).
 - [21] for a summary of recent results see e.g. S. Turyshev, Ann. Rev. Nucl. Part.Sci.**58**, 207 (2008)
 - [22] J. Williams, S. Turyshev and D. Boggs, Phys. Rev. Lett. **93**, 261101 (2004).
 - [23] B. Bertotti, L. Iess and P. Tortora, Nature **425**, 374 (2003).
 - [24] J. Levin, R. O'Reilly and E. Copeland, (Sussex U.), Phys. Rev. D **62** 024023 (2000).
 - [25] M.G. Germano, V.B. Bezerra, E.R. Bezerra de Mello (1997), Class. Quantum Grav **13** 2663 (1997)
 - [26] see e.g. S. Carroll, *Spacetime and Geometry: An Introduction to General Relativity*, Benjamin Cummings (2003).